Eur. Phys. J. E (2008)
DOI 10.1140/epje/i2007-10266-4

THE EUROPEAN PHYSICAL JOURNAL E

Thermal diffusion and bending kinetics in nematic elastomer cantilever

K.K. Hon, D. Corbett, and E.M. Terentjev[a]

Cavendish Laboratory, University of Cambridge, J.J. Thomson Avenue, Cambridge CB3 0HE, UK

Received 5 October 2007
Published online: 24 January 2008 –

Abstract. Vertically aligned monodomain nematic liquid-crystal elastomers contract when heated. If a temperature gradient is applied across the width of such a cantilever, inhomogeneous strain distribution leads to bending motion. We modelled the kinetics of thermally induced bending in the limit of a long thin strip and the predicted time variation of curvature agreed quantitatively with experimental data from samples with a range of critical indices and nematic-isotropic transition temperatures. We also deduced a value for the thermal diffusion coefficient of the elastomer.

PACS. 78.20.Hp Piezo-, elasto-, and acoustooptical effects; photoacoustic effects – 61.41.+e Polymers, elastomers, and plastics – 82.35.Ej Nonlinear optics with polymers – 83.80.Va Elastomeric polymers

1 Introduction

Liquid-crystal elastomers (LCE) combine the long-range orientational correlation of liquid crystals and entropically driven polymer elasticity to give a range of exotic properties such as spontaneous reversible shape changes and "soft elasticity" —deformation with no or little energy cost, leading to a variety of director instabilities under transverse extensions [1].

Nematic LCE possess the simplest uniaxial orientational order and can be synthesized by incorporating rod-like anisotropic mesogenic groups into the strands of weakly crosslinked polymer networks. The order is characterized by its principal axis, the nematic director $\boldsymbol{n}$, and the scalar order parameter $Q = \langle P_2(\cos\theta)\rangle$, which measures the mean orientation of mesogenic groups with respect to the director. Such an internal degree of freedom coupled to the elastic body constitutes what is known as the Cosserat medium: the relative movement of crosslinking points provides elastic strains and forces, while the director rotation causes local torques and couple-stresses —both intricately connected in the overall macroscopic response of the body. In fact, the physics of LCE is much richer than that of notional Cosserat solids because (again due to the entropic nature of long polymer chains connecting the crosslinking points) rubbers are capable of very large shear deformations (being at the same time essentially incompressible). Hence, one expects a variety of unique physical properties, especially in the region of large deformations. However, in this work we shall explore only small local strains.

Due to the coupling to the elastic body, the change in the degree of alignment of mesogenic rods leads to spontaneous elongation or contraction of the whole network along $\boldsymbol{n}$ as constituent polymer chains become on average more or less anisotropic (prolate or oblate depending on the system). This direct coupling between physical conformation and order parameter has been theoretically predicted a long time ago [2], and then comprehensively demonstrated by simultaneous measurements of length and order using diffraction techniques [3–5].

Landau theory predicts a 1st-order transition into the isotropic phase as the nematic LCE is heated above its nematic-isotropic transition temperature T_{NI}. This is based on the quadrupolar symmetry of the second-rank tensor order parameter of the nematic, which does not distinguish between rods pointing "upwards" and "downwards". However, in the elastomer network that was crosslinked in the aligned director state in order to obtain a permanent monodomain nematic texture [6], one does not find a discontinuous jump in the order parameter. Instead, frozen-in uniaxial stress leads to the supercritical continuous change of $Q(T)$ across the transition, and with it the continuous equilibrium uniaxial deformation of the monodomain nematic LCE. Depending on the degree of induced anisotropy of polymer chains forming the network, the magnitude of this deformation can be as high as 500% [7].

Spontaneous shape changes can also be induced optically. Photoelastomers doped with rod-like groups, such as azobenzene derivatives, which undergo *trans-cis*

[a] e-mail: emt1000@cam.ac.uk

isomerization on absorption of UV photons [8,9], or carbon nanotubes, which respond to IR light [10], are found to contract when irradiated at suitable wavelengths since local order is disrupted by the kinked dopant groups. Due to the high stroke and the equilibrium (reversible) nature of induced deformations, this now becomes an active area of engineering micro-optical mechanical systems (MOMS).

Inhomogeneous deformations are of special interest since they see potential applications in photo- and thermal actuators, detectors and sensors, microrheological valves and pumps, as well as structures which can respond to their neighboring environment. Non-uniform deformations occur when a spatial stress distribution is induced inside an elastomer. This could be achieved by irradiation, or by application of temperature gradient across the sample. Mathematical models [11] have been proposed to predict equilibrium curvatures in unilaterally illuminated photoelastomer cantilevers with exponential attenuation. However, in contrast to uniaxial contractions along the nematic director that have been well documented, no quantitative measurements have been made so far on bending curvatures. At the same time, while qualitative experiments on optically induced deformations have reported time scales varying from $< 100\,\mathrm{ms}$ [12] to $\sim$ 1–10 s [13, 14] depending on the incident intensity of light sources, the kinetic aspects of the bending motion have not been addressed theoretically.

This paper presents the first quantitative experimental study of the dynamics and kinetics of thermally induced bending in a nematic elastomer cantilever. We apply radiative heating to one side of cantilevers made from well-aligned monodomain polysiloxane side-chain elastomers, and measure the amplitude and time evolution of the induced curvature. We also develop a theoretical model, which predicts the reduced curvature of the cantilever as a function of time for cantilevers with different critical exponents, transition temperature and maximum strain. A value for the thermal diffusion coefficient of the elastomer is estimated from matching the model predictions to the experiment.

2 Experimental section

Materials. All side-chain siloxane liquid-crystalline elastomers, as well as their starting materials, were prepared in the Cavendish Laboratory following the procedures of Finkelmann *et al.* [6,15]. The polymer backbone was a poly-dimethylhydrosiloxane with approximately 60 Si-H units per chain, obtained from ACROS Chemicals. The pendant mesogenic group in sample A (NE-A) was purely 4-methoxyphenyl-4-(1-buteneoxy) benzoate (MBB), while sample B (NE-B) contained of 70 mol% of MBB and 20 mol% of 4-alkeneoxy-4′-cyanobiphenyl (ACB), as illustrated in Figure 1. All networks were chemically crosslinked via the same hydrosilation reaction in the presence of commercial platinum catalyst COD, obtained from Wacker Chemie, with di-functional crosslinking group 1,4 di(11-undecene) benzene (11UB) also synthesized in house. In all cases the crosslinking density

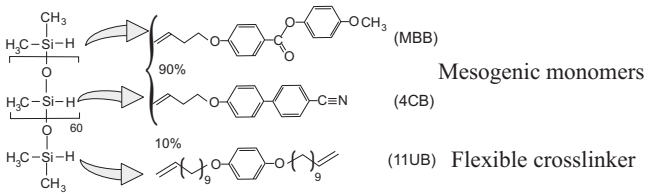

Fig. 1. Schematic illustration of the materials used in this work. Siloxane backbone chain with Si-H groups was reacting with 90 mol% mesogenic side groups and 10 mol% of flexible crosslinking groups (11UB). Two materials differed in the composition of mesogenic groups: NE-A had 90 mol% of MBB, while NE-B had 70 mol% of MBB and 20 mol% of ACB.

was 10 mol% of the reacting bonds in the siloxane backbone, so that on average each chain has 9 mesogenic groups between crosslinking sites. These materials have been very well studied over the years; both have a glass transition around 0 °C and nematic-isotropic transitions: $T_{NI} \approx 87\,^{\circ}\mathrm{C}$ for NE-A, and $T_{NI} \approx 101\,^{\circ}\mathrm{C}$ for NE-B.

Monodomain alignment. Monodomain, aligned samples of nematic elastomers were made by following the classical two-step crosslinking approach of Finkelmann *et al.* [6]. First we prepare partially crosslinked films in a centrifuge, highly swollen in toluene (2–3 ml per 1 g of material), reacting for 25–35 minutes at $\sim 75\,^{\circ}\mathrm{C}$ before evaporating the solvent and suspending the samples under load in an oven for more than 5 hours at 120 °C to complete the second-stage crosslinking reaction. A careful study of reaction kinetics ensured that approximately 50% of crosslinks were established in the first stage of this preparation. When a uniaxial stress is applied to such a partially crosslinked network, the uniaxially aligned state in the resulting nematic elastomer is established with the director along the stress axis. This orientation is then fixed by the subsequent second-stage reaction, when the remaining crosslinks are established.

Following the original ideas of [6] and the present understanding of the nature of polydomain nematic LCE [16], in all cases we performed the second-stage crosslinking in the high-temperature isotropic phase: only in this way a good alignment and mechanical softness are achieved (in contrast to crosslinking in a stretched polydomain nematic phase, which results in topological defects and localized domain walls frozen in the material).

The mechanical history of the samples was eliminated by annealing in the isotropic phase for > 2 hours ($\sim 130\,^{\circ}\mathrm{C}$) followed by slow cooling. A precise measurement of the variation in natural length $L(T)$ with temperature was then made with a travelling microscope, which followed the end points of a sample that was suspended without load and heated at a slow rate of $0.33\,^{\circ}\mathrm{C/min}$ in an insulated glass-front oven.

Measurements of the natural length $L(T)$ variation with temperature, Figure 2, were fitted to a model function $L/L_0 = 1 + \beta(1 - T/T_{NI})^a$, where L_0 is the constant length of samples in the isotropic phase. Obviously, such a superficially critical behavior cannot be matched to experiment at the transition point itself (where supercritical

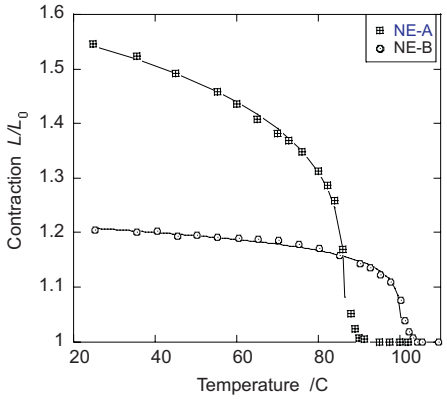

Fig. 2. Curves of equilibrium uniaxial contraction of monodomain nematic LCE. The two samples (labelled on the plot) have different transition temperatures T_{NI} and different chain anisotropy, leading to the 20% and 55% contraction, respectively. Solid lines drawn through the data below T_{NI} represent the analytical fit functions described in the text.

effects take over), but it provides a very good continuous interpolation of the data in the nematic phase. Fitting to the data gives $a = 0.25$, $\beta = 0.843$ and $T_{NI} = 359.6\,\mathrm{K}$ for NE-A, and $a = 0.21$, $\beta = 0.3$ and $T_{NI} = 373.8\,\mathrm{K}$ for NE-B.

The thickness w of the two samples (which we shall require in the cantilever analysis) was 0.351 mm (NE-A) and 0.368 mm (NE-B) at room temperature. Elastomer samples were cut into thin strips of approximate dimensions $L \times W \times w = 5\,\mathrm{mm} \times 1\,\mathrm{mm} \times w$ (with differing thickness) and had one end vertically attached to a stand on an adjustable platform. Sideways images of the strips (cantilevers) were taken by a Sanyo VCB-3512T monochrome CCD camera ($f = 9\,\mathrm{mm}$) with direct back lighting and digitally captured using software FTA32 by First Ten Angstroms Inc at a frame rate of 15 fps. An Antex CS 16W soldering iron provided heating. This soldering iron had a flat tip (cylinder of 4.5 mm diameter) which provided uniform radiative heating over the whole cantilever. Imaging of this tip also acted as a scale for confirming the thickness w of the samples by comparing dimensions on screen. The soldering iron, which was allowed to equilibrate for 15 minutes before each experiment, was mounted horizontally on a movable stand which can be slid to the desired position (2 mm) in front of the mounted sample in less than 0.2 s, which marked the start of each kinetic measurement. Temperatures at the front and the back of the samples were measured with a thermocouple, however, not during the cantilever-bending experiment (but in a separate event of heating in exactly the same conditions).

Movies of the bending motion were taken and each frame was analyzed both manually and using a MATLAB image-processing algorithm. Manually, the radius of curvature was obtained by superposing circles of various sizes on the outline of the curved sample using graphics software CorelDraw and adjusting until the circle of best fit was found, see Figure 3. The automated MATLAB algorithm extracted the position of points along the curved edge of the sample in the image and fitted the set of points

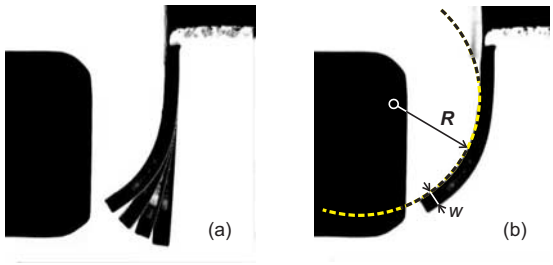

Fig. 3. (a) A composite image showing the extent of cantilever bending. On the left one can see the tip of the soldering iron. (b) The scheme of the manual analysis of the cantilever curvature.

to the equation of a circle with variable radius R by a least-squares method; the optimized value of R was then output as the radius of curvature. In the end, our procedure was to analyze all images in an automated way, but then re-examine every anomalous point manually (because we found that our algorithm was not coping well with the cases of non-uniform curvature along the cantilever). The outputs of this analysis were the values of normalized curvature w/R against time for each bending experiment.

3 Theoretical model

Heat diffusion across a flat strip.

The problem of thermal diffusion in a flat sample exposed to a constant heat flux from one side is certainly a classical one. We give its brief account here in order to expose the key parameters of the problem, required for the subsequent description of cantilever bending. Consider a 1D diffusion of the scalar temperature field $T(x,t)$ across the thickness of the cantilever, $\partial_t T = D\partial_x^2 T$, where the diffusion coefficient $D = \kappa/C$ is the ratio of thermal conductivity κ (given by the heat flux definition $J = -\kappa\partial_x T$) to specific heat capacity per unit volume C. We assume that the soldering iron acts as a source of constant flux J at $x = 0$, while losses on the front ($x = 0$) and back ($x = w$) surfaces are taken to be proportional to the difference between the temperature on the sides, T_f and T_b, and the ambient surrounding, T_0, *i.e.* $-\kappa\partial_x T = J - \gamma(T_\mathrm{f} - T_0)$ at $x = 0$, and $-\kappa\partial_x T = \gamma(T_\mathrm{b} - T_0)$ at $x = w$, taking flux to be positive to the right.

Since the diffusion equation consists only of derivatives of the temperature field T and the boundary conditions are only sensitive to temperature differences, we can homogenize the problem by considering the function $\theta = (T - T_0)$ instead. Introducing natural variables $\chi = x/w$ and $\tau = Dt/w^2$, the problem can be recast as

$$\partial_\tau\theta = \partial_\chi^2\theta\ , \quad \text{with} \begin{cases} \partial_\chi\theta = \Delta(\theta - \Theta_c) & \text{at } \chi = 0, \\ \partial_\chi\theta = -\Delta\,\theta & \text{at } \chi = 1, \\ \theta = 0 & \text{at } \tau = 0, \end{cases} \qquad (1)$$

where $\Delta = w\gamma/\kappa$ and $\Theta_c = J/\gamma$ are the two essential parameters of the problem.

In the steady state $\partial_\tau\theta = 0$. Being it a 1D problem, only a linear solution $\theta = A\chi + B$ could satisfy $\partial_\chi^2\theta = 0$.

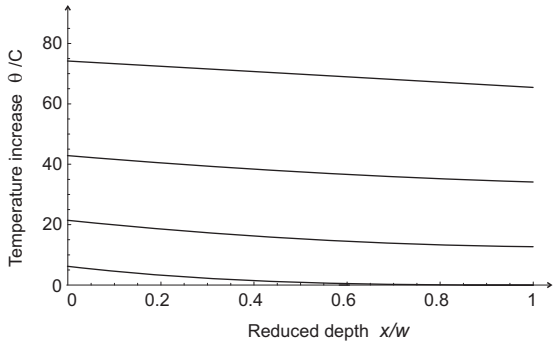

Fig. 4. Plots of $\theta = T - T_0$ across the cantilever thickness x/w. Increasing curves are for the times $Dt/w^2 = 0.1, 1, 3$ and 100.

Letting the steady-state front and back temperatures be and $T_{\rm f}^*$ and $T_{\rm b}^*$, respectively, (equivalently $\theta_{\rm f}^*$ and $\theta_{\rm b}^*$), the steady-state temperature profile across the sample is given by $\theta_{\rm s} = \theta_{\rm f}^* - (\theta_{\rm f}^* - \theta_{\rm b}^*)\chi$. Parameters Δ and Θ_c can then be expressed as

$$\Delta = (\theta_{\rm f}^*/\theta_{\rm b}^* - 1) \quad \text{and} \quad \Theta_c = (\theta_{\rm f}^* + \theta_{\rm b}^*), \tag{2}$$

which consist only of explicitly measurable quantities $T_{\rm f}$, $T_{\rm b}$ and T_0. Note that for a thin enough sample one expects $T_{\rm f}^* \approx T_{\rm b}^*$ and so $\Delta \ll 1$. The full time-dependent solution can be obtained by superposing a series of different time decay modes $\theta = A_k \sin(k\chi + \phi)\exp(-k^2\tau)$ on the steady-state solution. Quantization conditions for k and ϕ are determined by the initial/boundary conditions, giving the transcendental equations

$$k_n = \Delta \tan(n\pi/2 - k_n/2) \ \text{ and } \ \phi_n = (n\pi/2 - k_n/2) \tag{3}$$

for integer n. Fourier analysis of orthogonal modes in $\theta(\chi, \tau)$ gives the expression for coefficients,

$$\begin{aligned} A_n &= (-1)^{(n+1)/2}\frac{2\Theta_c \sin(k_n/2)}{k_n + \sin(k_n)} \quad \text{for odd } n; \\ &= (-1)^{n/2+1}\frac{2\Theta_c}{k_n}\frac{\Delta}{2+\Delta}\frac{k_n\cos(k_n/2) - 2\sin(k_n/2)}{k_n - \sin(k_n)} \end{aligned} \tag{4}$$

for even n. The full solution for the temperature across the sample of thickness w is therefore given by

$$\begin{aligned} T(x,t) = T_{\rm f}^* - (T_{\rm f}^* - T_{\rm b}^*)\frac{x}{w} \\ + \sum_{n=1}^{\infty} A_n \sin\left(k_n\left[\frac{x}{w} - \frac{1}{2}\right] + \frac{n\pi}{2}\right) e^{-k_n^2 Dt/w^2}. \end{aligned} \tag{5}$$

There are two features of this solution that we need for our main problem. First of all, there is a characteristic time scale in the problem, given by the ratio w^2/D which will allow us estimate the thermal diffusion constant in nematic LCE. Note that the $(n = 1)$ mode in equation (5) has $k_1 \approx \pi\Delta$ at $\Delta \ll 1$ and, therefore, this is the slow-decaying mode. Other modes have k_n of order $(n-1)\pi$ and decay fast, in practice, within a few seconds in our experiments.

The second aspect of the solution $T(x,t)$ is the rather smooth variation across the cantilever thickness. Figure 4 demonstrates the x-dependence at different times, which justifies an essential simplifying approximation made in the next section, taking $T(x)$ to be a simple linear function connecting the two values $T_{\rm f}$ and $T_{\rm b}$.

Kinetics of cantilever bending.

Consider now a long thin strip of elastomer, preferentially contracted at the front and bent accordingly, due to unilateral heating from the side $x = 0$ starting at $t = 0$. A temperature distribution $T(x,t)$ is set up across the cantilever thickness. Since the length of a monodomain nematic elastomer below T_{NI} is locally given by $L/L_0 = 1 + \beta(1 - T/T_{NI})^a$, the local strain distribution due to contraction along the z-direction (vertical in Fig. 3) can be calculated. Taking the zero-strain state at ambient temperature T_0, we obtain

$$\begin{aligned} \varepsilon(x) &= \frac{L(x)}{L(T_0)} - 1 \\ &= \frac{\beta}{[1 + \beta(1 - T_0/T_{NI})^a]}\left[\left(1 - \frac{T}{T_{NI}}\right)^a - 1\right], \end{aligned} \tag{6}$$

where $L(T_0)$ is the sample length at ambient temperature. Assuming Young's modulus to be constant over the temperature and strain range of the experiment, this strain can be directly converted to stress $\sigma = E\,\varepsilon(x)$, at each depth x into the sample. As the elastomer deforms incompressibly, a contraction in the z-direction would lead to transverse expansions along x and y. However, for the case of a long thin strip in which $L \gg W > w$, x- and y-curvatures can be safely ignored.

Let x_n be the position of a neutral plane [11]. Mechanical equilibrium requires, in the absence of external forces and torques, that force and moment vanish across every cross-section of the cantilever. This means that all bending stress, $E(x - x_n)/R$, where R is the radius of curvature of the beam, is provided by the excess stress $E[\varepsilon(x) - \varepsilon(x_n)]$ with respect to this neutral plane. Two conditions representing the balance of forces and torques are, as in [11],

$$\begin{aligned} \int_0^w W\,{\rm d}x\,E\frac{x - x_n}{R} &= \int_0^w W\,{\rm d}x\,E[\varepsilon(x) - \varepsilon(x_n)], \\ \int_0^w W\,{\rm d}x\,x\,E\frac{x - x_n}{R} &= \int_0^w W\,{\rm d}x\,x\,E[\varepsilon(x) - \varepsilon(x_n)], \end{aligned} \tag{7}$$

where W is the width of the cantilever (the y-dimension), Ww being the cross-section area of the beam.

Assuming a linear temperature drop across the thickness, $T(x) = T_{\rm f} - (T_{\rm f} - T_{\rm b})x/w$, the spatial integrals can then be conveniently converted to over temperature via ${\rm d}T = -(T_{\rm f} - T_{\rm b}){\rm d}x/w$ to obtain

$$\begin{aligned} \frac{1}{R}\left(\frac{w}{2} - x_n\right) &= \int_{T_{\rm b}}^{T_{\rm f}} \frac{\varepsilon(T)\,{\rm d}T}{T_{\rm f} - T_{\rm b}} - \varepsilon(x_n) \\ \frac{1}{R}\left(\frac{w}{3} - \frac{x_n}{2}\right) &= \int_{T_{\rm b}}^{T_{\rm f}} \frac{(T_{\rm f} - T)\varepsilon(T)\,{\rm d}T}{(T_{\rm f} - T_{\rm b})^2} - \frac{\varepsilon(x_n)}{2}. \end{aligned} \tag{8}$$

Note that both the lateral width W and the Young modulus E scale out of these mechanical balance equations. On elimination of x_n and $\varepsilon(x_n)$ from these two equations, one obtains

$$\frac{w}{R} = 12\int_{T_\mathrm{b}}^{T_\mathrm{f}} \frac{(T_\mathrm{f}-T)\varepsilon(T)\,\mathrm{d}T}{(T_\mathrm{f}-T_\mathrm{b})^2} - 6\int_{T_\mathrm{b}}^{T_\mathrm{f}} \frac{\varepsilon(T)\,\mathrm{d}T}{T_\mathrm{f}-T_\mathrm{b}}\,. \quad (9)$$

The problem could be solved completely if we had an analytical expression for $\varepsilon(T)$. Unfortunately, our interpolation formula is only applicable below T_{NI}, while above the transition ε is constant. The break at T_{NI} calls for a different mathematical treatment for the following two regimes:

i) When the temperature is below T_{NI} everywhere in the sample, $T_{NI} > T_\mathrm{f} > T_\mathrm{b}$, evaluating the integrals gives the dimensionless curvature:

$$\begin{aligned}\frac{w}{R} = {} & \frac{6\beta}{[1+\beta(1-T_0/T_{NI})^a]}\frac{1}{2+3a+a^2} \\ & \cdot\left[\frac{T_{NI}-T_\mathrm{f}}{T_\mathrm{f}-T_\mathrm{b}}\left(1-\frac{T_\mathrm{f}}{T_{NI}}\right)^a\left(2+a+2\frac{T_{NI}-T_\mathrm{f}}{T_\mathrm{f}-T_\mathrm{b}}\right)\right. \\ & \left. + \frac{T_{NI}-T_\mathrm{b}}{T_\mathrm{f}-T_\mathrm{b}}\left(1-\frac{T_\mathrm{b}}{T_{NI}}\right)^a\left(a-2\frac{T_{NI}-T_\mathrm{f}}{T_\mathrm{f}-T_\mathrm{b}}\right)\right]. \quad (10)\end{aligned}$$

Here T_f and T_b are independently measurable time-dependent functions. At all temperatures within this regime the curvature w/R is a monotonically increasing function of time with the positive second derivative (convex function).

ii) When the T_f exceeds T_{NI}, so that the phase transition front is inside the sample, $T_\mathrm{f} > T_{NI} > T_\mathrm{b}$, we obtain:

$$\begin{aligned}\frac{w}{R} = {} & \frac{6\beta}{[1+\beta(1-T_0/T_{NI})^a]}\frac{T_{NI}-T_\mathrm{b}}{T_\mathrm{f}-T_\mathrm{b}} \\ & \cdot\left(1-\frac{T_\mathrm{b}}{T_{NI}}\right)^a \frac{a+2(T_\mathrm{f}-T_{NI})/(T_\mathrm{f}-T_\mathrm{b})}{2+3a+a^2}. \quad (11)\end{aligned}$$

This expression represents a non-monotonic function of time, with the negative second derivative (concave function) and the maximum curvature w/R followed by a decrease when the majority of the sample becomes isotropic.

Regime ii) comes to an end when the temperature at the back of the cantilever, T_b, reaches the transition point T_{NI}, *i.e.* all of the sample becomes homogeneously isotropic. At this point, evidently, $w/R = 0$. Calculating the integrals in the regime when all of the sample is isotropic, $T_\mathrm{f} > T_\mathrm{b} > T_{NI}$, confirms that $w/R = 0$ at all times.

In our experiments the powerful heating flux has ensured that the temperature rise was high so the interesting regimes (i) and (ii) occurred at relatively short times, when both T_f and T_b were well approximated by a single exponential:

$$\begin{aligned} T_\mathrm{f} &= T_\mathrm{f}^* - (T_\mathrm{f}^* - T_0)e^{-t/\tau_\mathrm{f}}\,, \\ T_\mathrm{b} &= T_\mathrm{b}^* - (T_\mathrm{b}^* - T_0)e^{-t/\tau_\mathrm{b}}\,, \end{aligned} \quad (12)$$

where τ_f and τ_b are the effective thermal diffusion times at the front and back, respectively. It is expected that τ_f and τ_b take similar but not identical values, since inspection of the full series for $T(x,t)$ shows that the spatial coefficient of $\sin[k_n(x/w-1/2)+n\pi/2]$ is identical at $x=0$ and $x=w$ for odd modes, but swaps sign for even n. In this single-exponential approximation, regime changes occur at $t_1 = \tau_\mathrm{f}\ln(T_\mathrm{f}^*-T_0)/(T_\mathrm{f}^*-T_{NI})$, when the front of the elastomer enters the isotropic phase and the curve $w/R(t)$ has an inflection point; and at $t_2 = \tau_\mathrm{b}\ln(T_\mathrm{b}^*-T_0)/(T_\mathrm{b}^*-T_{NI})$, when the elastomer becomes uniformly isotropic and hence returns to a state of zero curvature, with also a zero tangent. The values and gradients of reduced curvature match on both sides of t_1 and t_2, as is physically required.

4 Analysis of bending kinetics

In both samples, the reduced curvature w/R variation is characterized by three distinct regimes. Immediately after the start of the experiment (heat flux on) there is a slow initial increase of curvature with time; this is followed by a sharp peak, after which the curvature rapidly dropped to zero. This trend corresponds to regimes i) and ii) described in the theoretical model, but also could be qualitatively understood by considering the shape of the contraction curve of the nematic elastomer, L/L_0 against T (see Fig. 2). Initially, when the sample is relatively far away from T_{NI}, the mechanical response to temperature change is flat. The local strains induced at the front and back surfaces are small and similar in magnitude. However, as the temperature approaches T_{NI}, which happens first on the front of the cantilever, the internal stress gradient is amplified by the increasing steepness of the $L(T)$ curve. This leads to the cantilever curvature rising at an increasing rate. The curvature will be decreasing again after the front portion of the cantilever turns isotropic and stops contracting while the on-going contraction at the back reduces the stress gradient. Finally, the sample returns to a stationary unbent state as it becomes uniformly isotropic.

Figures 5 and 6 show the measured values of curvature w/R. The solid line in each plot is the fit by the theoretical model, equations (10) and (11). Evidently, the agreement is very good, both qualitatively and quantitatively —except in the final stages of sample unbending, where the discrepancies are significant. This, however, should be expected because of the following two factors, one practical, the other to do with data analysis.

In our model, we have ignored the fact that, as curvature increases, the lower end of the cantilever lifts and becomes closer to the heat source. Figure 3 shows this very clearly. This introduces a significant deviation from the theoretical assumption in the model, that the heat flux J is constant. It is clear that, after the point of maximal bending is reached, the real heat flux on the sample is inhomogeneous along the length of the cantilever (z local coordinate). As a result, the far end of the cantilever (the part closest to the heat source) will become homogeneously isotropic much earlier than the simple 1D diffusion model would predict. In practice we see this very clearly, as in the final stages of the heating cycle the far end of the cantilever is already straight, while the middle and

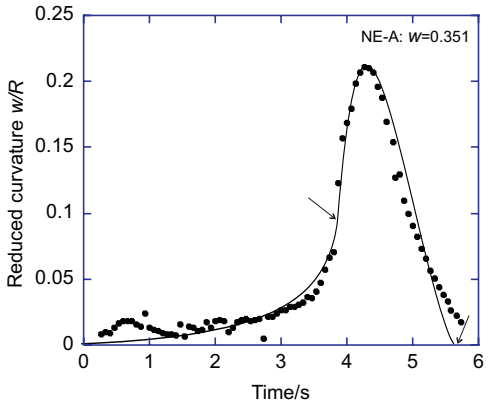

Fig. 5. Experimentally measured values of reduced curvature w/R, for the NE-A cantilever, against time after the start of heating. The solid line is the fit by theoretical equations (10) and (11), with arrows showing where regimes i) and ii) end.

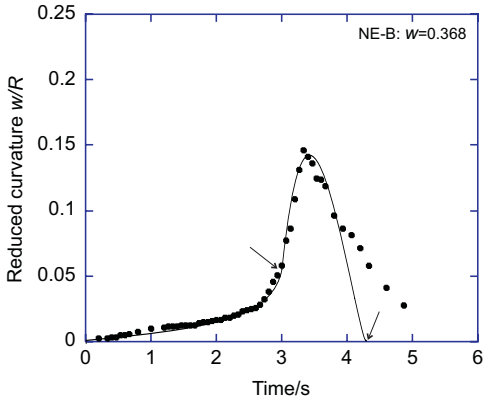

Fig. 6. Experimentally measured values of reduced curvature w/R, for the NE-B cantilever, against time after the start of heating. The solid line is the fit by theoretical equations (10) and (11), with arrows showing where regimes i) and ii) end.

near parts still have curvature remaining. Such buckling occurred more significantly in NE-B than in NE-A, as seen from the curvature plots, however in all cases both manual and algorithmic fitting was difficult and ambiguous as curvatures are no longer constant.

The other discrepancy factor is inherent in the model itself. In order to obtain closed-form expressions for $w/R(t)$, equations (10) and (11), we had to use an interpolating formula for the underlying thermal contraction $L(T)$. As is clear from Figure 2, this formula does not work in the immediate vicinity of the transition T_{NI}, where all materials show differing degree of diffuse supercritical behavior. So it is not surprising that the model expressions deviate from the actual data when the temperatures of the sample are around, or slightly above, the notional T_{NI}. These are the regions past the curvature peak, where the model "assumes" that the local regions with $T > T_{NI}$ are fully isotropic, while in practice we know that the contraction continues for 2–3 more degrees.

Among other ignored effects, which might become apparent at high temperatures (later times of the bending cycle) there is heating of surrounding air and lateral heat loss, which would require ambient temperature T_0 to be time dependent and a full 3D treatment of heat diffusion, respectively. All these factors could be eliminated or much reduced in impact. We could (and indeed have in some experiments) mount the heat source at an angle to minimize the effect of one cantilever end approaching it too closely. We could also write a much more elaborate interpolation formula to account for the full continuous $L(T)$ variation, and then proceed to calculate all integrals numerically. However, on reflection we have decided that the benefits of such improvements would not be worth the price of losing the simplicity of experiment and the ease of analysis. After all, the agreement of the model with experiment in the early regions of the bending process is excellent, as we expect when the material is in the nematic phase.

The point of maximum curvature occurred at 4.3 s for NE-A and at 3.3 s for NE-B. Since we have measured the saturation temperatures $T_{\rm f}^*$ and $T_{\rm b}^*$ independently, as well as determined the parameters β, a, T_{NI} of the intrinsic thermal contraction curves for each material, the only two fitting parameters are the front- and back-relaxation times $\tau_{\rm f}$ and $\tau_{\rm b}$, cf. equation (12). The best fits in Figures 5 and 6 were achieved with $\tau_{\rm f} = 2.42\,{\rm s}$ and $\tau_{\rm b} = 2.05\,{\rm s}$ for NE-A, and with $\tau_{\rm f} = 2.13\,{\rm s}$ and $\tau_{\rm b} = 2.5\,{\rm s}$ for NE-B. It must be remarked that despite the experimental and theoretical difficulties discussed above, the two-stage increase in the cantilever curvature shows good agreement with the experimental data. This proves that we understand the underlying physics of nematic elastomer cantilevers correctly, and allows us to extract relevant material parameters from the fits.

Parameters $\tau_{\rm f}$ and $\tau_{\rm b}$ can be viewed as a characteristic heating time for the sample. By comparison with the first terms of the thermal diffusion solution, equation (5), they are expected to be of order $w^2/k_1^2 D$. Steady-state temperatures $T_{\rm f}^*$ and $T_{\rm b}^*$ were measured to be 375 K and 365 K for NE-A, and 398 K and 390 K for NE-B, giving $\Delta = 0.89$ and 0.133, respectively. The value of k_1 can then be obtained from solving the transcendental equation (3) numerically (giving $k_1 = 0.419$ for NE-A and 0.511 for NE-B). Rearranging, the thermal diffusion coefficient is given by $D \sim w^2/k_1^2\tau$. A typical value of D is therefore estimated to be $\sim 1.5 \cdot 10^{-7}\,{\rm m}^2/{\rm s}$. We are not aware of any measurements of thermal diffusion in nematic LCE, but this estimate compares favorably with the literature values of $D = 1.1 \cdot 10^{-7}\,{\rm m}^2/{\rm s}$ for a crosslinked silicone elastomer [17], a value also consistent with uncrosslinked silicone polymer melts [18].

5 Conclusions

In this work we experimentally studied the time variation of the curvature of a long thin strip of an aligned monodomain nematic elastomer, for two samples differing in their transition (constitutive) behavior and shape dimensions. Associated theoretical analysis was able to quantitatively describe the data and reflect all characteristic trends. Fitting the data allowed us to deduce

characteristic time scales and estimate the thermal diffusion constant D of the siloxane elastomer.

To the best of our knowledge, this is the first quantitative study of thermal diffusion in nematic elastomers, as well as their cantilever bending due to induced inhomogeneous strains arising from unilateral radiative heating. Such controlled and reproducible bending is an important physical effect underlying many engineering applications. Perhaps more practically relevant is the photo-induced cantilever bending, where the local strains are induced due to the photoisomerization reaction in azobenzene derivatives [11–14,19]. Our experiments on photo-bending, analogous to the current work, will be reported elsewhere. Nevertheless, thermal bending is a fundamentally important effect where one tests the details of continuum mechanics, kinetics of local and global response, and the general understanding of the nematic elastomer state.

We wish to thank A.R. Tajbakhsh for the preparation of samples, M. Warner for useful discussions concerning the diffusion equation and C. Picard for assistance in MATLAB programming.

References

1. M. Warner, E.M. Terentjev, *Liquid Crystal Elastomers*, 2nd ed. (Clarendon Press, Oxford, 2007).
2. M. Warner, K.P. Gelling, T.A. Vilgis, J. Chem. Phys. **88**, 4008 (1988).
3. W. Kaufhold, H. Finkelmann, Makromol. Chem. **192**, 2555 (1991).
4. J. Küpfer, H. Finkelmann, Macromol. Chem. Phys. **195**, 1353 (1994).
5. A.R. Tajbakhsh, E.M. Terentjev, Eur. Phys. J. E **6**, 181 (2001).
6. J. Küpfer, H. Finkelmann, Macromol. Rapid Commun. **12**, 717 (1991).
7. S.V. Ahir, A.R. Tajbakhsh, E.M. Terentjev, Adv. Funct. Mater. **16**, 556 (2001).
8. H. Finkelmann, E. Nishikawa, G.G. Pereira, M. Warner, Phys. Rev. Lett. **87**, 015501 (2001).
9. P.M. Hogan, A.R. Tajbakhsh, E.M. Terentjev, Phys. Rev. E **65**, 041720 (2002).
10. S.V. Ahir, E.M. Terentjev, Phys. Rev. Lett. **96**, 133902 (2006).
11. M. Warner, L. Mahadevan, Phys. Rev. Lett. **92**, 134302 (2004).
12. M. Camacho-Lopez, H. Finkelmann, P. Palffy-Muhoray, M. Shelley, Nat. Mater. **3**, 307 (2004).
13. Y. Yu, M. Nakano, T. Ikeda, Nature **425**, 145 (2003).
14. N. Tabiryan, S. Serak, X.-M. Dai, T. Bunning, Opt. Express **13**, 7442 (2005).
15. H. Finkelmann, H. Greve, M. Warner, Eur. Phys. J. E **5**, 281 (2001).
16. S.V. Fridrikh, E.M. Terentjev, Phys. Rev. E **60**, 1847 (1999).
17. A.W. Broerman, D.C. Venerus, J.D. Schieber, J. Chem. Phys. **111**, 6965 (1999).
18. D.W. van Krevelen, *Properties of Polymers*, 3rd ed. (Elsevier, Amsterdam, 1990).
19. C.L.M. Harvey, E.M. Terentjev, Eur. Phys. J. E **23**, 185 (2007).